J. Fluid Mech. (1993), *vol.* 255, *pp.* 707–721

Interaction of two cavitation bubbles with a rigid boundary

By J. R. BLAKE[1], P. B. ROBINSON[1], A. SHIMA[2], AND Y. TOMITA[3]

[1]School of Mathematics and Statistics, University of Birmingham, Edgbaston, Birmingham, B15 2TT, UK

[2]Institute of Fluid Science, Tohoku University, Sendai, Japan

[3]Hakodate College, Hakkaido University of Education, Hakodate, Japan

(Received 23 October 1992 and in revised form 2 June 1993)

The motion of two cavitation bubbles near a rigid boundary is observed experimentally using a high-speed camera and compared against numerical solutions obtained using a boundary integral method. The comparisons are favourable with regard to both bubble shape history and centroid motion. The bubbles show a range of responses depending on the experimental configuration. Elongated bubbles, jets directed towards or away from the rigid boundary and bubble splitting phenomena are all observed and predicted for the given parameters. It is clear that nearby bubbles are equally as important as the presence of a rigid boundary in determining the behaviour of bubbles.

1. Introduction

In most practical situations bubbles do not occur in isolation (e.g. cavitation, boiling, chemical reactors) but exist in large numbers. Clearly it is important to understand the mechanics of bubble interaction as well as their response to the ambient flow field and nearby boundaries. The effects of nonlinear interactions on the motion of both bubble and a nearby free surface have been studied in several previous papers (Blake, Taib & Doherty 1986, 1987). The behaviour of non-spherical bubbles near boundaries yields a range of bubble shapes, in some cases leading to the fragmentation of bubbles in the very late stages of collapse (see e.g. Plesset & Chapman 1972; Voinov & Voinov 1977; Robinson, Blake & Kucera 1993). In this paper we present an experimental and theoretical study of the interaction of two bubbles with a rigid boundary in an axisymmetric configuration. The study reveals the wide range of responses that may be found when bubble interactions are strong, clearly indicating the significance of including the dynamics of bubble interaction in any large-scale model of two-phase flow.

In the next section a brief summary of the modified experimental apparatus is presented together with a selection of different experimental observations that are analysed in greater detail in a later section when compared to the numerical model of §3. A modified boundary integral method is developed that allows the technique to be used for multiple bubble systems. The theory incorporates 'bubble splitting' phenomena to yield additional bubbles provided the flow domain remains simply connected (i.e. theory does not admit toroidal bubbles with circulation).

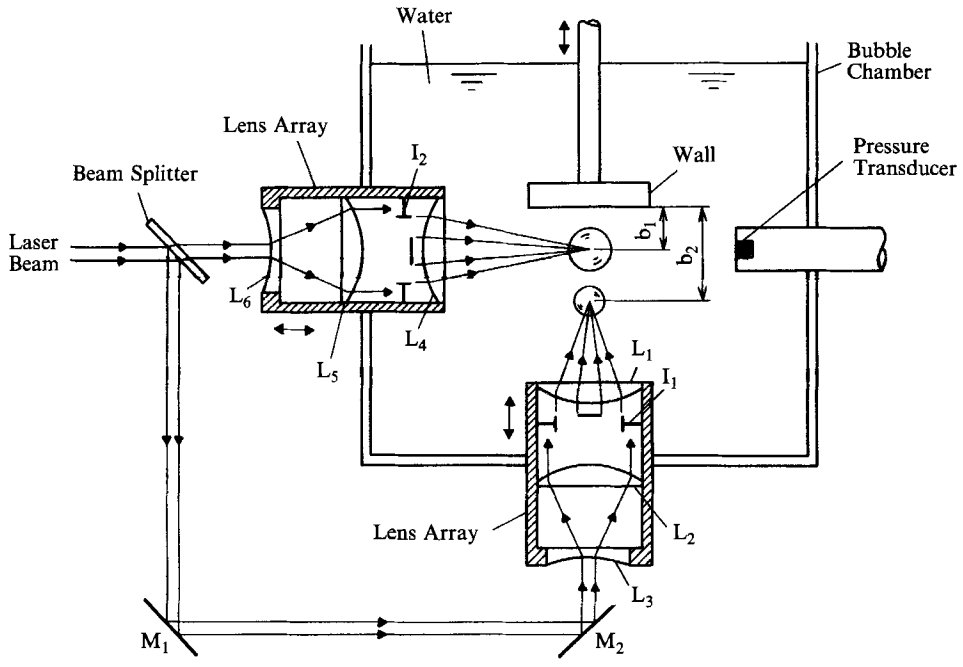

FIGURE 1. A schematic illustration of the experimental apparatus.

In §4 comparisons between experiment and theory are presented for the case of two axisymmetric bubbles. The accuracy of an earlier theory, reported in Vogel, Lauterborn & Timm (1989), is again confirmed by the studies reported in this paper. Section 5 compares theory and experiment, showing more clearly the effects that bubble interactions may have on each other's behaviour. It is clear that the interaction between bubbles is dependent on inter-bubble distance and is of equal importance as the presence of nearby boundaries.

2. Experiment

2.1. *Apparatus and techniques*

Bubbles were produced by focusing a ruby laser, with pulse width of approximately 20 ns and maximum power 60 MW, into water at room temperature (Tomita & Shima 1990). About 4 mJ of light energy was needed to produce a bubble with radius 1 mm. A schematic diagram of the test section is illustrated in figure 1. The laser beam was divided with a beam splitter: one beam entered a bubble chamber from the left and the other from below through two mirrors. Each beam was enlarged to twice its original size and cut with an iris as well as a small, circular stop after collimating. Finally they were both focused with two aspheric lenses, each with focal length of 12 mm in air, into tap water to produce two bubbles simultaneously. A single bubble may be obtained by cutting one branch of the beams. The position of bubble production is adjustable by controlling two lens arrays, which enable us to obtain two bubbles at arbitrary points on a focal plane. A transparent acrylic plate was used as a solid wall to prevent unnecessary bubbles forming due to the heat absorbed by a laser beam while passing through the wall. The wall was positioned from the upper part or side of the chamber for each experimental situation.

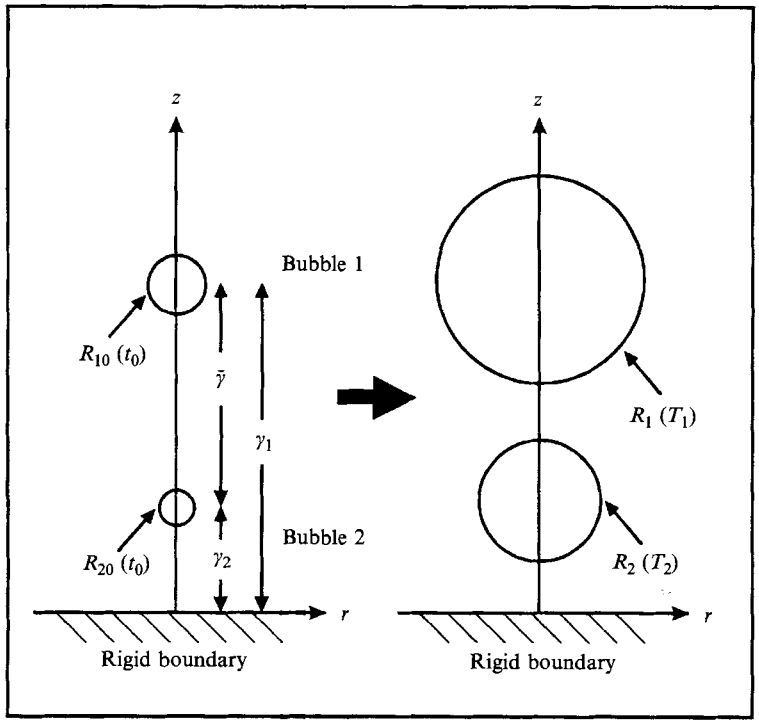

FIGURE 2. A schematic illustration of the axisymmetric geometry used in consideration of the motion of two cavitation bubbles near a rigid boundary.

The motion of bubbles was observed using an Imacon high-speed camera (John Hadland 790) with framing rate of 100 000 frames s^{-1} and exposure time of 2 μs frame^{-1}. The location of the camera would be depicted above the plane of figure 1. A diffuser was placed behind the focal plane to visualize the bubble interiors. The timing of the photography was adjusted with a delay circuit.

2.2. *Observations*

In the experimental observations reported in this paper we restrict the study to axisymmetric configurations of (i) a cavitation bubble near a horizontal rigid boundary, and two cavitation bubbles in (ii) an effectively infinite fluid and (iii) directly above one another near a horizontal rigid boundary.

In describing the geometrical arrangement of the bubbles near a rigid boundary (see figure 2), we denote the larger of the two bubbles as 'bubble 1' and smaller of the two bubbles as 'bubble 2'. We define the lengthscale R_1^*, by

$$R_1^* = \max\left[\frac{3}{4\pi}V_1^*(t)\right]^{\frac{1}{3}}, \tag{1}$$

where R_i^* $(i = 1, 2)$ is the equivalent radius of 'bubble i' at maximum volume. If b_i $(i = 1, 2)$ is the distance above the boundary where the laser beams are focused then we define the dimensionless location and radius parameters as

$$\gamma_i = \frac{b_i}{R_1^*}, \qquad R_2 = \frac{R_2^*}{R_1^*}, \qquad R_1 = 1 \tag{2}$$

with $0 < R_2 \leqslant 1$. The dimensionless separation distance of the two bubbles is denoted

Figure	γ_1	γ_2	$\bar{\gamma}$	R_2
7(*a*)	1.30	-	-	-
7(*b*)	0.84	-	-	-
8(*a*)	-	-	3.34	0.91
8(*b*)	-	-	2.49	0.47
9(*a*)	0.99	3.60	2.61	0.94
9(*b*)	4.38	1.73	2.65	0.96
9(*c*)	6.23	3.19	3.04	0.98
10(*a*)	2.17	0.47	1.70	0.57
10(*b*)	2.27	0.67	1.60	0.49
10(*c*)	3.59	1.39	2.20	0.61

TABLE 1. Dimensionless form of the experimentally measured data used in the calculations

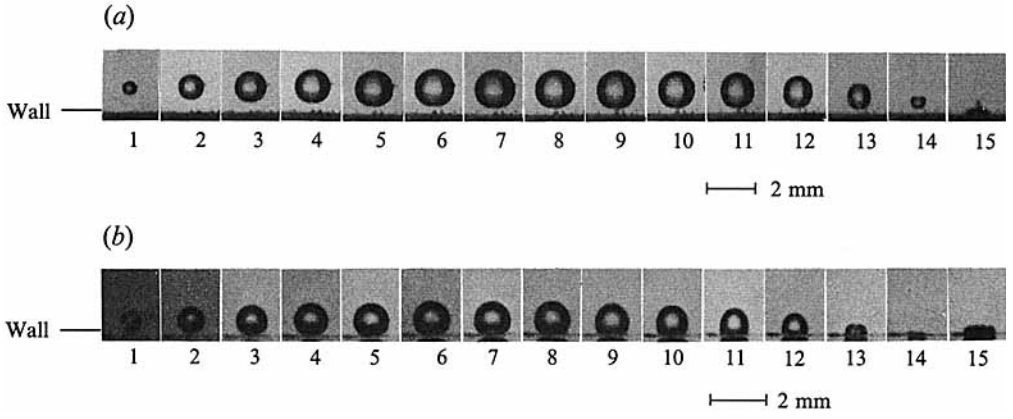

FIGURE 3. High-speed photographs of a single bubble near a rigid boundary.

by $\bar{\gamma} = |\gamma_2 - \gamma_1|$. Details of the experimentally measured parameters and the data used in the numerical calculations are recorded in table 1. In this study it is also assumed that both bubbles are generated at the same instant.

Figure 3 shows photographs of two examples of a single bubble generated at different distances from a plane rigid wall. This is the situation described in many previous studies (Plesset & Chapman 1971; Lauterborn & Bolle 1975; Tomita & Shima 1986; Blake *et al.* 1986; Vogel *et al.* 1989). We can see a familiar process of the bubble motion, covering growth and collapse phases. Non-spherical flow is induced when a bubble oscillates near a rigid boundary, and subsequently the bubble deforms. Eventually a high-speed liquid microjet, directed towards the wall, is formed in the latter stage of the bubble collapse.

The simplest example of the interaction of two bubbles is the case without a solid wall. High-speed photographs covering the whole period of bubble motion are shown in figure 4 for (*a*) similar-sized and (*b*) different-sized bubbles. The distance between bubbles and individual bubble size, which is proportional to the period of the bubble motion, are found to be important factors affecting their mutual interaction. The translational motion is rapidly induced when each bubble becomes small in size. A counter-jet is visible in the rebound process of a smaller bubble in both figure 4(*a*),

(*a*)

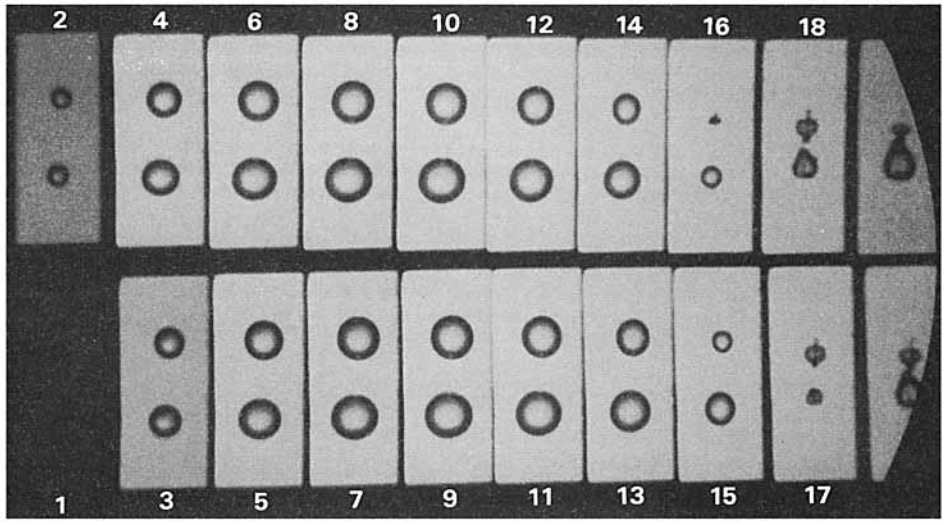

(*b*)

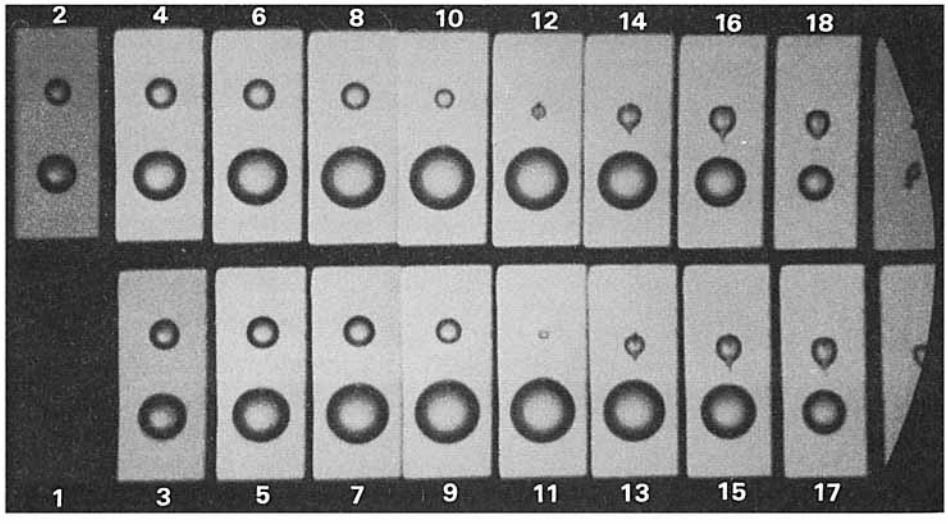

2 mm

FIGURE 4. High-speed photographs of two bubbles in an effectively infinite fluid with (*a*) similar-sized bubbles and (*b*) different-sized bubbles.

after the 17th frame, and figure 4(*b*), after the 14th frame. Observations reported here are in agreement with earlier studies by Timm & Hammitt (1971) and Lauterborn & Hentschel (1985). The earlier work of Timm & Hammitt showed evidence of counter-jet development in equi-sized bubbles, although in their study it appears at the second rebound. It is not clear if the counter-jet in the smaller bubble is associated with the

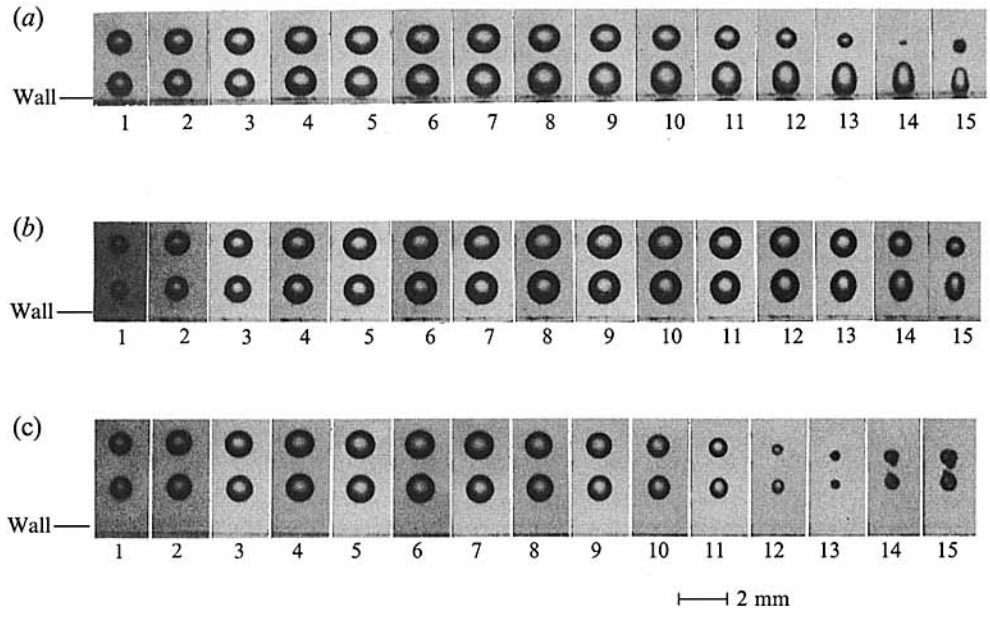

FIGURE 5. High-speed photographs showing three examples of two approximately equal-sized bubbles near a rigid boundary.

shock wave generated by the larger bubble on collapse or due to the coalescence of the toroidal bubble on rebound.

Series of photographs of the axisymmetrical motion of two bubbles, which are generated in a column perpendicular to a wall, are shown in figures 5 and 6. We found that there are various features of bubble motion that depend on parameters such as bubble size, distance between bubbles and distance from each bubble to a wall.

In figure 5 the behaviour of two approximately equal-sized bubbles (i.e. $R_2 \approx 1$) is shown for various values of the parameters γ_1 and γ_2. Figures 5(*a*) and 5(b) show elongations of the bubble nearer to the wall during the collapse phase. Figure 5(*c*) records the case where both bubbles are located further from the boundary, increasing the importance of the mutual bubble interaction.

A very interesting and important phenomenon is observable in figure 6 for the case where the bubble nearer to a wall is smaller than that further from the wall. Figures 6(*a*) and 6(*b*) record the response where the smaller bubble is again elongated during its early collapse phase. In the latter case necking of the elongated bubble is clearly visible which finally separates the upper and lower sections of the bubble, forming two smaller bubbles. In the next section the boundary integral method is extended to allow consideration of multi-bubble models and to provide further insight into bubble–boundary interactions and the observed 'bubble splitting' phenomena. Figure 6(*c*) records the case where both bubbles are initially located further from the boundary than the other examples in this figure. However the elongation of the smaller bubble indicates that it is subject to strong interactions with both the rigid boundary and the larger bubble above it, although ultimately it migrates towards the larger bubble.

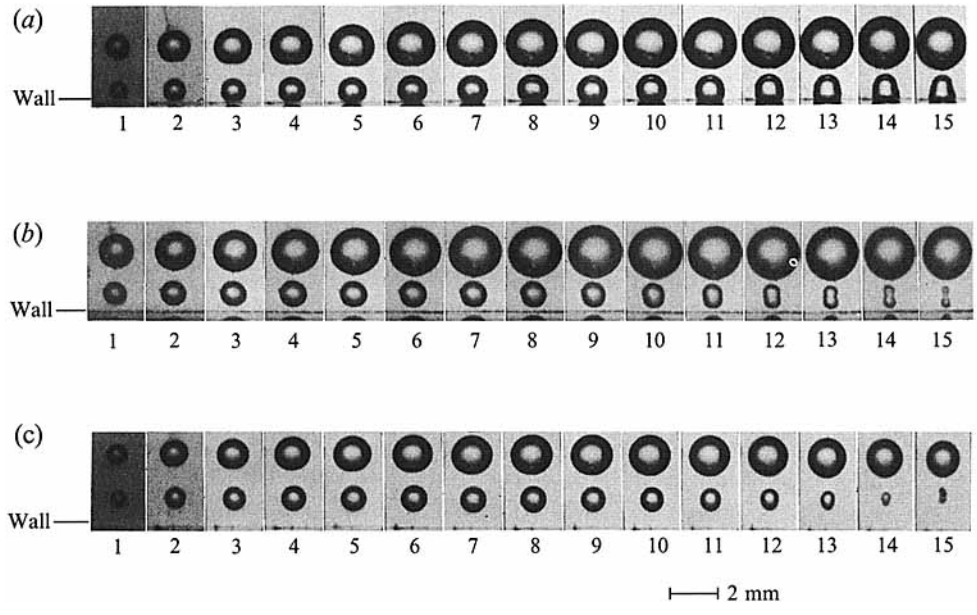

FIGURE 6. High-speed photographs showing three examples of two different-sized bubbles near a rigid boundary.

3. Theory

The fluid volume Ω surrounding the bubbles is assumed inviscid and incompressible, and motion irrotational, leading to the fluid velocity $\boldsymbol{u}$ being expressed as the gradient of a potential ϕ, i.e.

$$\boldsymbol{u} = \nabla\phi, \tag{3}$$

with ϕ satisfying Laplace's equation in the fluid;

$$\nabla^2\phi = 0. \tag{4}$$

During the process of inception, each bubble is assumed to originate from a small gas nucleus and subsequently grow to many times its initial volume. If this growth is so rapid that mass-diffusion effects are negligible, the gas content of each bubble plays no appreciable role in the dynamics until late in the final collapse phase. We therefore assume that bubbles are composed predominantly of vapour.

The ambient fluid pressure p_∞ is high compared to surface tension effects, while the pressure at the bubble interfaces is assumed constant and equal to the saturation vapour pressure p_v. Due to the small lifetime and volume associated with the growth and collapse of a cavitation bubble the effects of buoyancy can also be neglected.

With the above assumptions, the dynamic boundary condition on the bubble surfaces can be written

$$\Delta p = \rho\frac{\partial\phi}{\partial t} + \tfrac{1}{2}\rho|\boldsymbol{u}|^2, \tag{5}$$

where Δp is given by

$$\Delta p = p_\infty - p_v. \tag{6}$$

The previously defined maximum bubble radius R_1^* allows the introduction of the following dimensionless variables given in terms of the characteristic collapse velocity

$(\Delta p/\rho)^{\frac{1}{2}}$ by

$$\bar{t} = \frac{t}{R_1^*}\left(\frac{\Delta p}{\rho}\right)^{\frac{1}{2}}, \quad \bar{\phi} = \frac{\phi}{R_1^*}\left(\frac{\rho}{\Delta p}\right)^{\frac{1}{2}}, \quad \bar{p} = \frac{p - p_v}{\Delta p}. \tag{7}$$

Dropping bars, (6) yields the rate of change of potential at the surfaces,

$$\frac{\mathrm{D}\phi}{\mathrm{D}t} = \tfrac{1}{2}|\boldsymbol{u}|^2 + 1. \tag{8}$$

Fluid particles initially on the bubble surfaces S_i $(i = 1, 2)$ remain there, yielding the kinematic condition

$$\frac{\mathrm{d}\boldsymbol{p}}{\mathrm{d}t} = \nabla\phi, \quad \boldsymbol{p} \in S_i. \tag{9}$$

Application of Green's theorem in the three-dimensional domain leads to the boundary integral formulation given by

$$c(\boldsymbol{p})\phi(\boldsymbol{p}) = \sum_{i=1}^{2} \int_{S_i} \left(G(\boldsymbol{p}, \boldsymbol{q}) \frac{\partial \phi(\boldsymbol{q})}{\partial n} - \phi(\boldsymbol{q}) \frac{\partial G(\boldsymbol{p}, \boldsymbol{q})}{\partial n} \right) \mathrm{d}S_i(\boldsymbol{q}) \tag{10}$$

with

$$c(\boldsymbol{p}) = \begin{cases} 1, & \boldsymbol{p} \in \Omega, \\ \frac{1}{2}, & \boldsymbol{p} \in S_i. \end{cases}$$

When considering motion in an infinite fluid G is given by the free-space Green's function

$$G(\boldsymbol{p}, \boldsymbol{q}) = \frac{1}{4\pi|\boldsymbol{p} - \boldsymbol{q}|}, \tag{11}$$

and when considering motion in the neigbourhood of a rigid boundary, we choose

$$G(\boldsymbol{p}, \boldsymbol{q}) = \frac{1}{4\pi}\left\{ \frac{1}{|\boldsymbol{p} - \boldsymbol{q}|} + \frac{1}{|\boldsymbol{p} - \boldsymbol{q}'|} \right\}, \tag{12}$$

where $\boldsymbol{q}'$ is the image of $\boldsymbol{q}$ reflected about the boundary thus immediately satisfying the no-flow condition through the rigid boundary.

Initially we assume that the action of the focused laser is to yield a vapour bubble which expands spherically, unperturbed by the presence of other boundaries, to some small radius R_{0i} at time t_0 as shown in figure 2. Initial trials using an appropriate Rayleigh bubble potential to produce bubbles of equivalent radii R_i proved unsatisfactory for the case $R_2 < 1$, due to the interaction which takes place with the larger bubble during the growth phase. For the case $R_2 = 0.5$ initially prescribed with $\bar{\gamma} = 2.0$, the measured value of R_2 is underestimated by approximately 7% whereas R_1 is overestimated by approximately 3%. This effect is further increased when bubble 2 is placed adjacent to a rigid boundary, further impeding its radial motion. To calculate the required initial potential ϕ_{0i} to a high degree of accuracy, a Newton–Raphson scheme is employed to match the required values of R_i at each bubble's respective maximum volume. Denoting $\boldsymbol{J}$ as the Jacobian matrix, the iterative scheme

$$\boldsymbol{\phi}_0^{k+1} = \boldsymbol{\phi}_0^k - \left[\boldsymbol{J}^{-1}\right]^k \left(\boldsymbol{R} - \boldsymbol{R}^k\right), \qquad k = 0, 1, \ldots \tag{13}$$

is used, where the boundary integral method is utilized to evaluate the maximum equivalent radii R_i^k at each iteration. As an initial approximation $\boldsymbol{\phi}_0^0$ we choose the

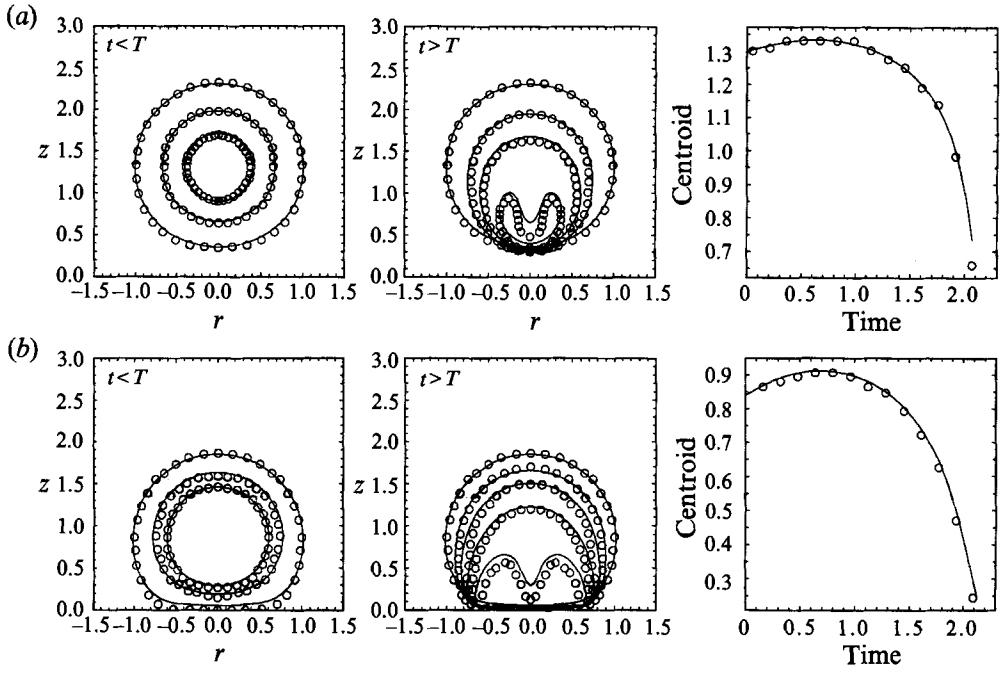

FIGURE 7. Numerically calculated bubble shapes and centroid positions of a single bubble near a rigid boundary for (*a*) $\gamma = 1.30$ and (*b*) $\gamma = 0.84$, with comparisons to the experimental results of figure 3 (circles).

Rayleigh potentials

$$\phi_{0i}^{0}(t_0) = -R_{0i}\left[\frac{2}{3}\left(\frac{R_i^3}{R_{0i}^3} - 1\right)\right]^{\frac{1}{2}}, \tag{14}$$

where t_0 is evaluated in terms of an incomplete Beta funcion

$$t_0 = 3\left(\frac{3}{2}\right)^{\frac{1}{2}} B_{R_{01}^3}\left(\frac{5}{6}, \frac{3}{2}\right), \tag{15}$$

and

$$R_{0i} = R_{01} R_i. \tag{16}$$

The procedure is iterated until the maximum error in R_i^k is less than 0.5%, which is typically satisfied by $k = 3$. With the initial potentials prescribed, the bubbles subsequently expand to their maximum volumes with equivalent radii R_i at times $t = T_i$ given approximately by the half-period of a Rayleigh bubble,

$$T_i = 3\left(\frac{3}{2}\right)^{\frac{1}{2}} B\left(\frac{5}{6}, \frac{3}{2}\right) R_i \approx 0.915 R_i. \tag{17}$$

To solve (10) we employ a collocation method and represent the bubble surfaces by a number of Lagrangian particles. To overcome the non-smooth nature of the piecewise linear interpolations, cubic splines are used to interpolate both ϕ and S_i between node points. Further details of the numerical implementation may be found in Kucera (1992) and Best & Kucera (1992)

With ϕ and S_i known at time t, (10) can be solved as a Fredholm integral equation

of the first kind for the normal fluid velocity $\partial\phi/\partial n$ on the bubble surfaces. With the prior knowledge of ϕ on S_i, $\partial\phi/\partial s$ is also calculated leading to the fluid velocity $\boldsymbol{u}$ at the bubble surfaces. Equations (8) and (9) are integrated employing a second-order Runge–Kutta scheme to obtain ϕ and S_i at time $t + \delta t$. The above procedure is applied iteratively thus yielding the time evolution of the bubble configuration. Nodal redistribution and smoothing is applied periodically. Smoothing of ϕ and S_i is carried out using quadratic interpolation to alternate between a set of $N_i + 1$ node points and a set of N_i node points situated midway along individual arclengths.

In the next section comparisons are made between this theory and the experimental observations reported in §2.

4. Comparison between theory and experiment

In figure 7 comparison between the predictions of the numerical model and the measured bubble shape and centroid motion of figure 3 are shown. It is readily seen that both results are in good agreement except over a short period in the very final stage of collapse when the shape is deforming extremely rapidly and experimental data are less accurate. Due to the zero flux condition on the rigid boundary, the bubble centroid migrates marginally away from the boundary during the growth phase. However during the collapse phase the bubble centroid moves increasingly rapidly towards the rigid boundary as a result of momentum conservation. Ultimately this leads to the formation of the high-speed liquid jet that is directed towards the boundary.

In figure 8 comparisons of both bubble shape and centroid motion are made for the two-bubble example in an infinite fluid that was recorded in figure 4. In figures 4(*a*) and 8(*a*), the bubbles are of similar size ($R_2 = 0.91$) with the upper, smaller bubble (bubble 2) collapsing first, generating a broad jet directed towards the lower bubble. This feature is not evident in figure 4(*a*) but can be inferred from the penetrating jet that can be observed in the rebounding bubble of frames 17–18. These calculations are not capable of predicting the counter-jet clearly evident in the experiments; as indicated earlier, this jet is most likely associated with the shock wave generated at collapse of the larger bubble or reconnection of the expanding toroidal bubble. There is a strong mutual attraction of both bubbles in this case as is clearly evident from the centroid migration. In figures 4(*b*) and 8(*b*) the uppermost bubble (bubble 2) is much smaller ($R_2 = 0.47$), again collapsing first with a fine jet directed towards the lower bubble. Experimentally this is observed around frame 14 where the penetrating jet is again evident. The bubbles are weakly attracted towards each other, the smaller one more so during the latter stages of collapse, although the larger bubble is yet to collapse.

In figure 9 comparisons of both bubble shape and centroid motion are made for case of two approximately equal-sized bubbles near a rigid boundary with $R_2 \geqslant 0.94$ as recorded in figure 5. The bubble shapes illustrated in figure 9(*a*) would indicate that the lower bubble (bubble 1), which is of similar size to bubble 2, perceives the upper bubble as an almost identical one; thus effectively acting as an 'image system' for a rigid boundary. This being the case, the high-speed jet is directed towards the lower bubble and, as a consequence of the geometry, the rigid boundary. The lower bubble grows almost spherically but during collapse it behaves as if it were located between two parallel rigid boundaries and as a consequence of the flow, collapses from the side, yielding the elongated bubble shape so clearly evident in both experiment (frames 12–15) and in the theoretical calculations. If the calculations or

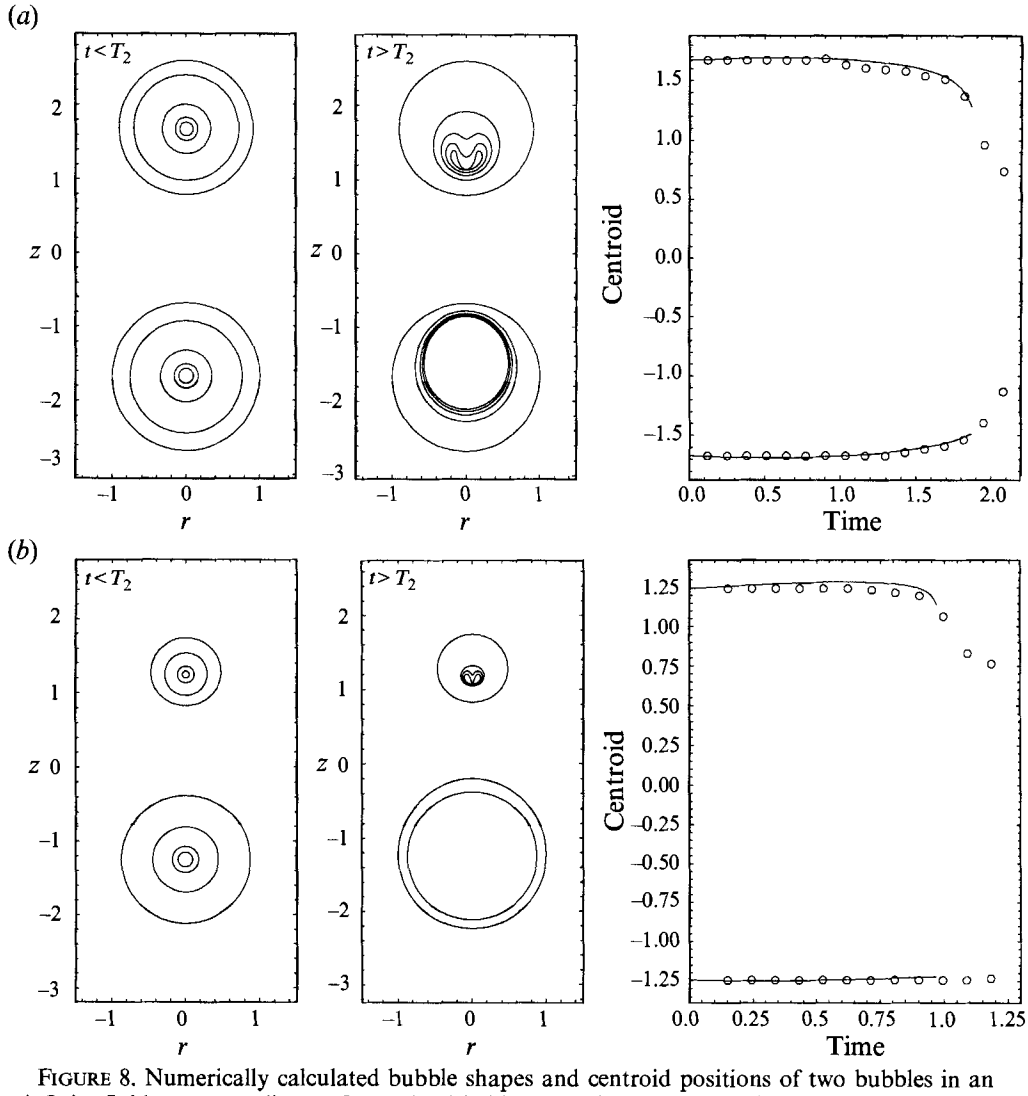

FIGURE 8. Numerically calculated bubble shapes and centroid positions of two bubbles in an infinite fluid corresponding to figure 4, with (*a*) $\bar{\gamma} = 3.34$, $R_2 = 0.91$ and (*b*) $\bar{\gamma} = 2.49$, $R_2 = 0.47$.

observations were to proceed further we would observe a strong sideways 'annular' jet that would ultimately split the lower bubble in two. The other significant factor is that the lifetime of the lower bubble adjacent to the wall is longer than that of the upper bubble due the reduced in-flow from above and below. This may have important consequences in terms of a 'cascade' of high pressures developing near a rigid boundary as bubbles finally collapse.

Figures 5(*b*) and 9(*b*) show an initial configuration of the system located slightly further from the boundary. The lower bubble (bubble 2) again elongates but this time retains much of its vertical symmetry due to the increased mobility of fluid from below. During its collapse phase this bubble migrates very slightly away from the rigid boundary. In this case however, the experimental record is not as long as that obtained from the numerical simulation which records the high-speed jet developed by the upper bubble.

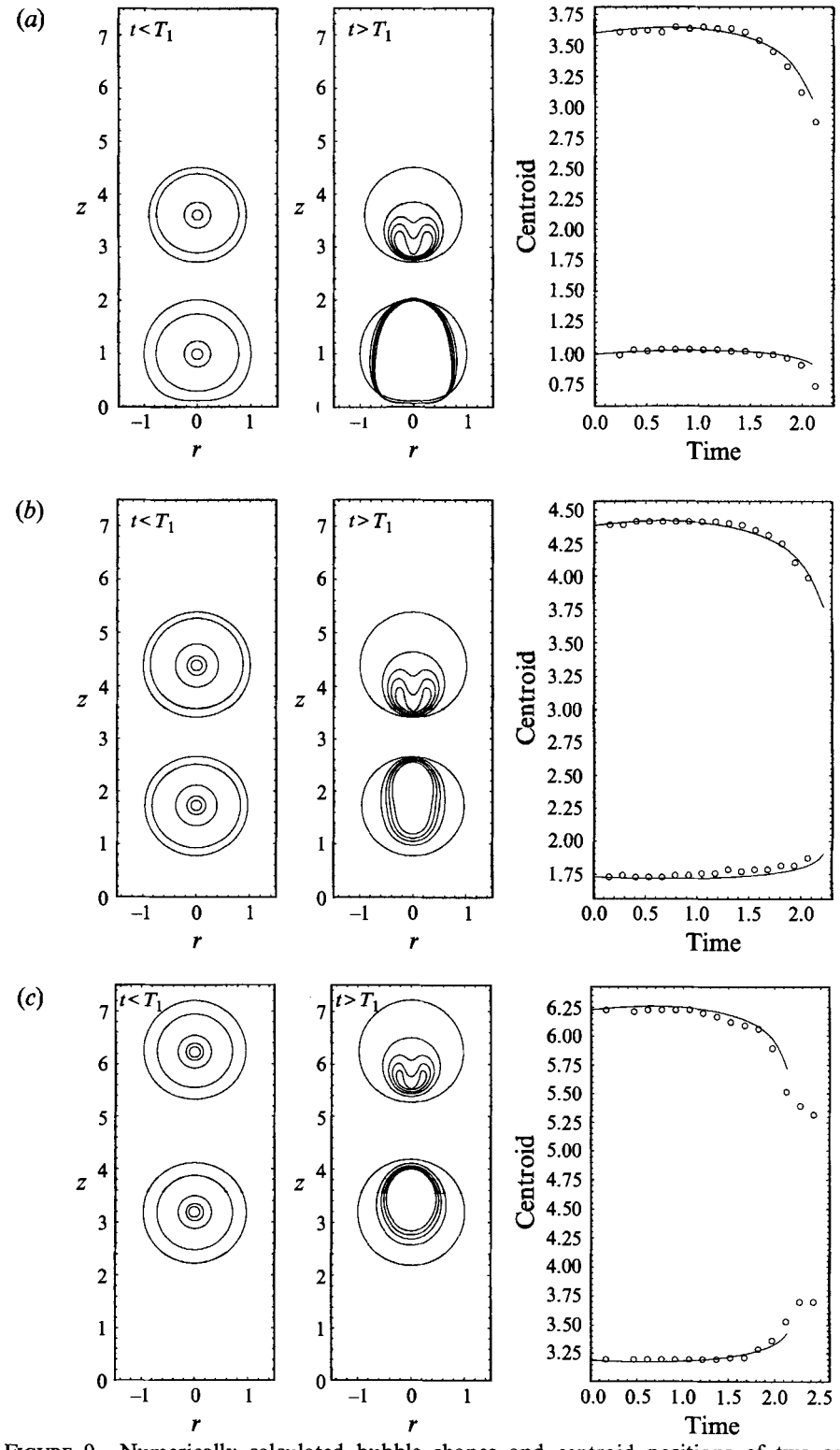

FIGURE 9. Numerically calculated bubble shapes and centroid positions of two approximately equal-sized bubbles near a rigid boundary corresponding to figure 5, with (*a*) $\gamma_1 = 0.99$, $\gamma_2 = 3.60$, $R_2 = 0.94$, (*b*) $\gamma_1 = 4.38$, $\gamma_2 = 1.73$, $R_2 = 0.96$, and (*c*) $\gamma_1 = 6.23$, $\gamma_2 = 3.19$, $R_2 = 0.98$.

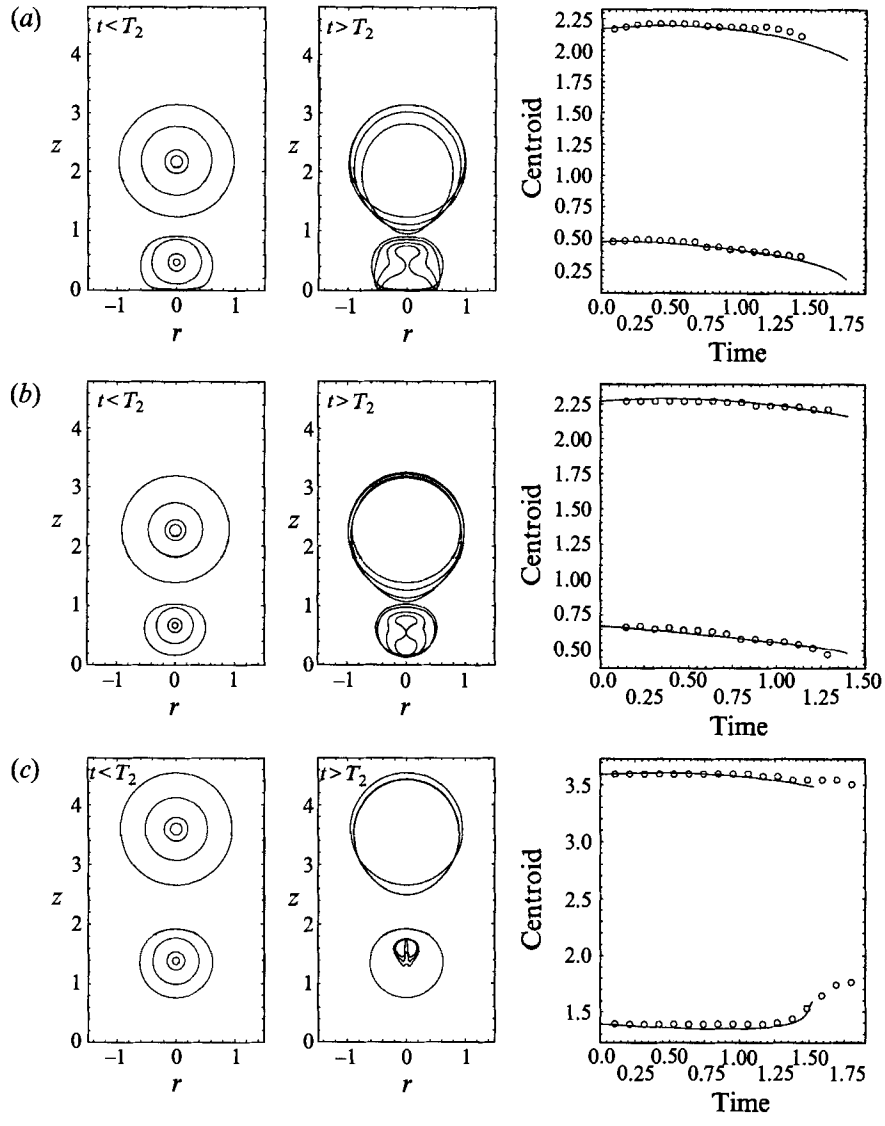

FIGURE 10. Numerically calculated bubble shapes and centroid positions of two different-sized bubbles near a rigid boundary corresponding to figure 6, with (*a*) $\gamma_1 = 2.17$, $\gamma_2 = 0.47$, $R_2 = 0.57$, (*b*) $\gamma_1 = 2.27$, $\gamma_2 = 0.67$, $R_2 = 0.49$, and (*c*) $\gamma_1 = 3.59$, $\gamma_2 = 1.39$, $R_2 = 0.61$.

In figures 5(*c*) and 9(*c*), two almost equal-sized bubbles are observed at some distance from the rigid boundary, at least in the sense that the strongest fluid mechanical interaction is with each other rather than the rigid boundary. Due to the increased spacing between the bubbles and boundary, the lower bubble (bubble 2) retains a more spherical shape with both bubbles collapsing on a comparable timescale. Both the bubble shape and centroid motions record movement towards each other, with high-speed liquid jets following this attraction. Clearly they are behaving as images for each other or, in other words, effectively as if there were a rigid boundary between them.

In figure 10 comparisons of both bubble shape and centroid motion are made

for cases where bubble 2 is located adjacent to the boundary with $R_2 \leqslant 0.61$ as recorded in figure 6. In figures 6(*a*) and 10(*a*), the lower bubble is initiated very close to the boundary. During the growth phase, the centroid position of the bubble is shown to migrate marginally towards the boundary due to the strong outward radial flow associated with the upper bubble. At maximum volume the lower bubble has expanded to take on a flattened profile located on the boundary. During the collapse phase, as in figure 9(*a*) the fluid flow near the lower bubble directed parallel to the boundary is far less restricted than that normal to the boundary. This effect produces a reduced inward motion of fluid at the lower section of the upper bubble with the formation of a pronounced protrusion, and the production of an annular jet around the surface of the lower bubble. Due to the lower inertia associated with fluid motion between the bubbles, as compared to the rigid boundary, the fluid flow towards the upper part of the lower bubble is greater than that towards its lower part. The formation of an annular jet is therefore stronger at the upper section of the bubble, causing this region to collapse faster, resulting in accelerated centroid migration towards the boundary. At time $t = 1.76$, pinch-off is observed to occur, and the lower bubble splits in two. Had the calculation been allowed to continue, two high-speed axial jets emanating from the high-curvature regions of closure would be formed, the lower of which would strike the boundary with an ultra high velocity.

In figures 6(*b*) and 10(*b*), the lower bubble is initiated further from the boundary, expanding more spherically towards maximum volume. During the majority of its lifetime, the bubble migrates towards the boundary under the strong influence of the radial motion of the upper bubble. During the collapse phase, the lower bubble is positioned approximately half way between the boundary and the lower surface of the upper bubble. In this case the flow field in the neighbourhood of the lower bubble is more symmetrical and the formation of an annular jet occurs around the equator. The centroid calculations show that the lower bubble again migrates towards the boundary which, due to the symmetrical collapse, occurs at approximately constant velocity. At closure of the neck, pinch-off occurs forming two small, nearly equal-sized bubbles.

In figures 6(*c*) and 10(*c*), the two bubbles are initiated further from the rigid boundary. In this case, much like the last, the smaller bubble retains much of its symmetry during expansion and early collapse phases. Upon collapse, the lower bubble again takes on an elongated form due to an increased mobility of fluid from the sides. In this instance however the distance between the two bubbles is far less than that between the boundary and the lower bubble. Therefore, with the increased importance of the two-bubble interaction, and the increased mobility of fluid from beneath the lower bubble, collapse occurs from below. The lower bubble therefore migrates towards the upper bubble, collapsing at its lower end yielding a 'cone-shaped' bubble. At this high-curvature region the lower bubble subsequently produces a high-speed axial jet penetrating the bubble from bottom to top.

5. Conclusions

It is clear from these observations that many types of behaviour can occur when the competing effects of a bubble interacting with both another bubble and a rigid boundary occur. Even within the relatively simple geometry used in the experiments and theory of this paper, a wide range of migratory behaviour and jet formation is found. Clearly, when bubbles are close together their mutual interactions can

dominate over the presence of a rigid boundary. These factors can influence the direction of migration and lifetime of the bubbles.

The numerical technique outlined in §3 can easily be utilized to calculate the bubble interaction for a finite number of bubbles near a rigid boundary. Although the axisymmetric arrangement is only likely to occur in very special circumstances, it does highlight the importance of the interaction with the nearest bubble or boundary.

The authors wish to acknowledge with thanks the contributions of Dr A. Kucera, Dr K. Sato and Mr N. Miura.

REFERENCES

BEST, J. P. & KUCERA, A. 1992 A numerical investigation of non-spherical rebounding bubbles *J. Fluid Mech.* **245**, 137–154.

BLAKE, J. R., TAIB, B. B. & DOHERTY, G. 1986 Transient cavities near boundaries. Part 1. Rigid boundary. *J. Fluid Mech.* **170**, 479–497.

BLAKE, J. R., TAIB, B. B. & DOHERTY, G. 1987 Transient cavities near boundaries. Part 2. Free surface. *J. Fluid Mech.* **181**, 197–212.

CHAPMAN, R. B. & PLESSET, M. S. 1972 Non-linear effects in the collapse of a nearly spherical cavity in a liquid *Trans. ASME* D: *J. Basic Engng* **94**, 142–146

KUCERA, A. 1992 A boundary integral method applied to the growth and collapse of bubbles near a rigid boundary *J. Comput. Phys.* (submitted).

LAUTERBORN, W. & BOLLE, H. 1975 Experimental investigations of cavitation bubble collapse in the neighbourhood of a solid boundary. *J. Fluid Mech.* **72**, 391–399.

LAUTERBORN, W. & HENTSCHEL, W. 1985 Cavitation bubble dynamics studied by high speed photography and holography. Part 1. *Ultrasonics* **23**, 260–268.

PLESSET, M. S. & CHAPMAN, R. B. 1971 Collapse of an initially spherical vapour cavity in the neighbourhood of a solid boundary. *J. Fluid Mech.* **47**, 283–290.

ROBINSON, P. B., BLAKE, J. R., & KUCERA, A. 1993 Collapse of non-spherical bubbles. (To be submitted.)

TIMM, E. E. & HAMMITT, F. G. 1971 Bubble collapse adjacent to a solid wall, a flexible wall and a second bubble. *AMSE Cavitation Forum*, pp. 18–20.

TOMITA, Y. & SHIMA, A. 1986 Mechanisms of impulsive pressure generation and damage pit formation by bubble collapse. *J. Fluid Mech.* **169**, 535–564.

TOMITA, Y. & SHIMA, A. 1990 High-speed photographic observations of laser-induced cavitation bubbles in water. *Acustica* **71**, 161–171.

TOMITA, Y., SHIMA, A. & TAKAHAHSI, H. 1991 The behaviour of a laser-produced bubble near a rigid wall with various configurations. *ASME Cavitation '91*, vol. 116, pp. 19–25.

VOGEL, A., LAUTERBORN, W. & TIMM, R. 1989 Optical and acoustic investigations of the dynamics of laser-produced cavitation bubbles near a solid boundary. *J. Fluid Mech.* **206**, 299–338.

VOINOV, V. V. & VOINOV, O. V. 1976 On the process of collapse of a cavitation bubble near a wall and the formation of a cumulative jet. *Sov. Phys Dokl.* **20**, 133–135.